COO-2315-8

Anisotropic Quasiparticle Properties in Aluminum*

A.B. Meador† and W.E. Lawrence

Department of Physics

Dartmouth College

Hanover, N.H.

October 1976

DISCLAIMER

ABSTRACT

We have studied the electron-phonon interaction in aluminum using Fermi-surface-fitted 4-OPW electron states, a realistic phonon spectrum, and integration mesh-density varying with local Fermi surface curvature. The resulting electron mass enhancement λ and thermal scattering rate τ^{-1} are evaluated as functions of position on the Fermi surface, with the following results: 1. The agreement between observed and calculated cyclotron masses is improved slightly by the use of our anisotropic λ rather than the average one, 2. The anisotropy of λ is determined predominantly by mixing coefficient variations, rather than by phonon anisotropy, 3. The scattering rate τ^{-1} exhibits order-of-magnitude variations over the Fermi surface at low temperatures. Its values at 5K are within 50% of the experimentally observed ones everywhere, with considerably better agreement in free-electron regions. 4. Deviations from the naively-expected T^3 behavior are predicted: In free-electron regions, umklapp processes cause a more rapid increase than T^3 for temperatures above 15-25K. On ridges, where the initial "T^3-coefficient" is very large, we find a slower increase. There results a washing-out of anisotropy with increasing temperature. The results on λ are in good agreement with those of a recent similar calculation; the τ^{-1} results agree qualitatively but not quantitatively.

I. Introduction

The continuing growth in capability to measure and analyze the scattering rates of quasiparticle excitations in metals[1,2] is exciting for a number of reasons, of which two are: 1. The scattering rate τ^{-1}, together with the effective mass enhancement λ, are basic to the description[3,4] of low-lying electronic excitations in the interacting electron-phonon system, and 2. The quasiparticle rate τ^{-1} is a uniquely sensitive probe of the anisotropy of the electron-phonon interaction -- anisotropy which manifests itself less directly in other quantities such as transport coefficients.[5] To amplify on the last statement, the electrical conductivity (for example) may be written as an average of the anisotropic transport relaxation time τ_{tr}. Although its anisotropy gives rise to dramatic effects, it cannot be measured directly, and at best only its qualitative features may be inferred from experimental data. So transport coefficients are rather insensitive probes of anisotropy.

In this paper we are concerned with the calculation of the quasiparticle properties, λ and τ, of aluminum. The reason for the choice is that aluminum presents the interesting combination of a multisheeted Fermi surface with a very simple electronic structure. (its electronic properties, including Fermi surface shape, are well-described by Ashcroft's 4-OPW model.[6]) Because of this simplicity the nature of the electron states is intimately related to the Fermi surface shape: single-OPW states in spherical regions, 2-OPW in most of the high-curvature regions (near zone boundaries), and 4-OPW near the zone corners. Certain features of the

quasiparticle properties might therefore be dictated by the surface shape.

The ingredients in this calculation are discussed in detail in sec. II, and so we state them only briefly here for comparison with previous calculations. The 4-OPW model is used for both the Fermi surface shape and the electron-phonon matrix elements, and a realistic phonon spectrum is used as well for the latter. The quasiparticle quantities are then calculated by direct integration over the Fermi surface, using a fixed mesh whose point-density is determined by local Fermi surface curvature. This calculational program and a somewhat similar one by Leung[7] differ from all previous aluminum calculations[8] in their detailed treatment of the electron structure. This program differs from Leung's in two respects: 1) Leung uses 15-OPW electron states and the Heine-Abarenkov pseudopotential for the calculation of matrix elements, and 2) Rather than doing surface integrals directly, he introduces the frequency distribution functions $\alpha^2F(\vec{k},\omega)$[7,8] as an intermediate step. The general agreement between our calculated values of λ suggests that the matrix elements are not seriously affected by the use of one method over the other. The discrepancy which exists between the τ values probably arises from the difference between our integration methods, since it is difficult in either case to treat low-frequency phonons with a high degree of accuracy. This problem will be discussed at length later.

In the remainder of this section we review the surface-integral expressions for λ and τ. First consider the simpler quantity λ; recall that it relates the quasiparticle velocity

$$\vec{v}_Q(\vec{k}) = [1 + \lambda(\vec{k})]^{-1} \vec{v}(\vec{k}) \tag{1}$$

to the bare "band" velocity $\vec{v}(\vec{k})$. It is given by the Fermi surface integral[3]

$$\lambda(\vec{k}) = \frac{1}{4\pi^3} \int \frac{dS'}{\hbar|\vec{v}'|} \sum_\sigma \frac{|g_\sigma(\vec{k},\vec{k}')|^2}{\omega_{q\sigma}} \tag{2}$$

where

$$|g_\sigma(\vec{k},\vec{k}')|^2 = (2\rho\omega_{q\sigma})^{-1} |\langle\vec{k}'|\hat{\varepsilon}_{q\sigma}\cdot\nabla V|\vec{k}\rangle|^2 \tag{3}$$

is the squared amplitude for the electron transition $\vec{k}\to\vec{k}'$, with the emission or absorption of a phonon with wavevector $\vec{q}$ and polarization σ. (for an emitted phonon, $\vec{q} = \vec{k}-\vec{k}'$ reduced to the first Brillouin zone) In (3), ρ is the mass density of aluminum, V is the Ashcroft pseudopotential (for consistency with the Fermi surface fit), and of course $\omega_{q\sigma}$ and $\hat{\varepsilon}_{q\sigma}$ are the phonon frequency and polarization, respectively. A similar formula holds for the thermal quasiparticle relaxation rate at the Fermi surface ($\varepsilon = 0$)[3]

$$\tau^{-1}(\vec{k},\varepsilon=0) = \frac{1}{\pi^2} \int \frac{dS'}{\hbar|\vec{v}'|} \sum_\sigma |g_\sigma(\vec{k},\vec{k}')|^2 f(\hbar\omega_{q\sigma}/k_B T) \tag{4}$$

where

$$f(x) = (e^x - 1)^{-1} (1 + e^{-x})^{-1} = n(x)[1 - f^\circ(x)]$$

incorporates the temperature-dependence through the equilibrium Fermi and Bose functions f° and n; note that f(x) falls off exponentially for large x. For quasiparticles <u>off</u> the Fermi surface the relaxation rate

$\tau^{-1}(\vec{k},\epsilon)$ is slightly more complicated than (4). For the measurements done in aluminum[9] the appropriate quantity is the average of $\tau^{-1}(\vec{k},\epsilon)$ over energies near the Fermi level, as discussed in a number of places,[4,10] and that is simply

$$\langle\tau^{-1}(\vec{k})\rangle \equiv \int_{-\infty}^{\infty} d\epsilon \left(-\frac{\partial f^{\circ}(\epsilon)}{\partial\epsilon}\right) \tau^{-1}(\vec{k},\epsilon)$$

$$= \frac{12}{7}\,\tau^{-1}(\vec{k},\,\epsilon = 0) \qquad (5)$$

related to the value at the Fermi level. Later we compare experimental measurements with $\langle\tau^{-1}(\vec{k})\rangle$, (5), rather than (4).

One further point must be discussed here. For very low temperatures the occupation factors f(x) restrict important contributions to the integral in (4) to the immediate vicinity of $\vec{k}$ (i.e. $|\vec{k}' - \vec{k}| \ll k_F$). The result is that, for any fixed integration mesh, the numerical sum intended to represent (4) approaches zero exponentially [exp(- c/T)], rather than algebraically (T^3) as does the exact integral (4), in the limit $T \to 0$. However the exact low-temperature limit may be calculated by writing the surface integral in plane polar coordinates

$$dS' \to q\,dq\,d\theta \qquad (T \to 0)$$

and observing the asymptotic form

$$\lim_{\vec{k}'\to\vec{k}} \frac{|g_{\sigma}(\vec{k},\vec{k}')|^2}{\omega_{q\sigma}} \equiv \lim_{\vec{k}'\to\vec{k}} G_{\sigma}(\vec{k},\vec{k}') = G_{\sigma}(\theta)\ , \qquad (6)$$

(this independence of G_σ on q will be demonstrated explicitly later) which permits the integrals to factorize. It is then elementary to show that

$$\lim_{T\to 0} \tau^{-1}(\vec{k}, \epsilon = 0) = \frac{2.104}{\pi^2 \hbar^4 |\vec{v}|} (k_B T)^3 \int_0^{2\pi} d\theta \sum_\sigma G_\sigma(\theta)\, C_\sigma^{-2}(\theta), \qquad (7)$$

where $C_\sigma(\theta)$ is defined by $\lim_{q\to 0} \omega_{q\sigma}(\theta) = q\, C_\sigma(\theta)$. The angular integral may be done numerically, to provide the exact T^3-coefficient for the low-temperature limit. This procedure will be discussed further in sec. II, along with many other details of the computations. The results of the calculations of both λ and τ^{-1} are given in sec. III.

II. The Calculations.

In this section we describe the method used to perform the Fermi surface integrations required in (2), (4), and (7), and we discuss the calculation of the necessary ingredients in the integrands. The integration mesh is shown on Fig. 1. It consists of 1294 points: 873 on the second zone hole surface, and 421 on the third zone electron surface. The mesh-point-density is greatest near the zone edges, where the curvature is high; the density was chosen to satisfy a criterion based on the electron-phonon matrix element variation (to be discussed later). It is apparent that the density is sufficient to represent the Fermi surface shape adequately. The points are located, and the wavefunctions are calculated by means of Ashcroft's four-OPW model. This model provides an excellent fit to the actual Fermi surface shape,[6] and we believe that it gives the wavefunctions to a sufficiently high level of accuracy that they are not a

limiting factor in the overall accuracy of the calculation.

For each mesh point, we calculate the element of surface area and the velocity $\vec{v} = \hbar^{-1}\vec{\nabla}_k \varepsilon$. These are then used to evaluate three surface integrals of interest, two of which are related to the "specific heat" and "optical" effective masses, as shown in Table I.

The matrix elements (3) required for the quasiparticle properties are calculated using the 4-OPW wavefunctions of the Ashcroft model, and a phonon spectrum derived from a Born-von Karman force constant fit to neutron data. The rationale for using the simple 4-OPW model for the matrix elements is as follows: First, we recall that Ashcroft's model is empirical, in the sense that the measured Fermi surface dimensions are used to infer the band gaps V(G). These band gaps are the values of the electron-ion form factor at the reciprocal lattice points $\vec{G} = [111]$ and $\vec{G} = [200]$. The form factor represents the electron-ion pseudopotential operator V -- the same V which occurs in the electron-phonon matrix elements (3). For consistency, then, the matrix elements should be calculated from a pseudopotential which "reproduces" Ashcroft's empirical band gaps, and from the same 4-OPW wavefunctions used in their determination.

In connection with the choice of form factor, we should point out that the usual Ashcroft form[11] is used, but with the ionic core parameter R_c set at 0.61 Å, rather than the 0.59 Å quoted in ref.11. This choice is necessary

in order to fit the empirical band gaps; it fits V_1 essentially exactly and overestimates V_2 by 13%. In contrast, the choice $R_c = 0.60$ Å underestimates V_1 seriously (~35%), while $R_c = 0.62$ Å overestimates both V_1 and V_2.

We have studied extensively the variation of the quantity $G_\sigma(\vec{k},\vec{k}') \equiv \omega_{q\sigma}^{-1} |g_\sigma(\vec{k},\vec{k}')|^2$ (the integrand of λ, see eqn. 2) over the Fermi surface, particularly in the vicinity of ridges. Through this study we developed the criterion for mesh density that the quantity $G_\sigma(\vec{k},\vec{k}')$ should vary by no more than 10% under the displacement of its arguments by a single interval in any direction. This criterion supplements the more subjective one that the mesh accurately represent the Fermi surface shape. As a result, there are relatively small regions, near the centers of ridges, where the 10% criterion becomes the determining factor for mesh density. The highest density is required near the narrow ridge which (on the second zone surface) joins the hexagonal and square regions. We call this the "V_1-ridge" since it is determined by the smaller of the two band gaps, $V_1 \equiv V(G=[111])$. The wider "V_2-ridge" ($V_2 \equiv V(G=[200])$ joins two hexagonal regions of the 2nd zone, and requires mesh-density only slightly greater than that used in free-electron (1-OPW) regions near L and X. The third zone arms of the Fermi surface consist largely of ridges, and therefore they require dense mesh everywhere; as a result, the third zone accounts for roughly one-third of the total number of mesh points (see Fig. 2).

Although the 10%-criterion is important only near the ridges, it is still responsible for the large number of mesh points, because so many of them (about two-thirds of the total number) occur near ridges. The mesh

pictured in Figs. 1 and 2 is ultimately a compromise between accuracy (10%-criterion), computer run-time (to compute λ at a single point requires about 3000 sec), and program cumbersomness (the mesh consists of seven separate regions - three on the second zone and four on the third zone).

Now we return to the point raised at the conclusion of sec. I - the problem of calculating τ^{-1} at very low temperatures. When typical thermally-occupied phonon wavevectors are comparable with or smaller than the mesh-point separations, the strict mesh-summation no longer represents the integral (3). However, in the low-temperature limit, τ^{-1} depends only on the gradients of the mixing coefficients (evaluated at the initial point $\vec{k}$), and on the directional sound velocities $C_\sigma(\theta)$. These gradients may be evaluated with the use of the mesh points neighboring the initial state, and so the calculation is relatively simple. The actual expression for τ^{-1} in the low-temperature limit may be derived by expanding the matrix element in (3):

$$\frac{1}{i}\langle\vec{k}'|\hat{e}_{q\sigma}\cdot\nabla V|\vec{k}\rangle = \hat{e}_{q\sigma}\cdot\sum_{i=1}^{4}\sum_{j=1}^{4}\alpha_i\beta_j^{*}(\vec{k}-\vec{G}_i-\vec{k}'+\vec{G}_j)\,V\,(\vec{k}-\vec{G}_i-\vec{k}'+\vec{G}_j)\,, \qquad (8)$$

where α_i and β_j are the mixing coefficients of the 4-OPW states, e.g. $|\vec{k}\rangle = \sum_{i=1}^{4}\alpha_i|\vec{k}-\vec{G}_i\rangle$, and $V(p) \equiv \langle\vec{q}|V|\vec{q}+\vec{p}\rangle$ is the matrix element of the (local) pseudopotential V between single-OPW states $|\vec{q}+\vec{p}\rangle$ and $|\vec{q}\rangle$. In the limit $\vec{k}'\to\vec{k}$ we are of course considering an intraband process, so that α_j and β_j have the same functional form $\alpha_j(\vec{k})$, and

$$\beta_j(\vec{k}') = \alpha_j(\vec{k}) + (\vec{k}'-\vec{k}) \cdot \nabla\alpha_j(\vec{k}) \quad . \tag{9}$$

Retaining only the lowest order terms in the phonon wavevector $q = k-k'$ we end up with (neglecting the $\partial V(p)/\partial p$ term[12])

$$\frac{1}{i} \langle\vec{k}'|\hat{\varepsilon}_{q\sigma} \cdot \nabla V|\vec{k}\rangle = \varepsilon_{q\sigma} \cdot [\vec{q}\, V(o) + \sum_{i<j} \vec{A}_{ij}\, q\, V(\vec{G}_i-\vec{G}_j)] \quad , \tag{10a}$$

where

$$\vec{A}_{ij} = (\vec{G}_i-\vec{G}_j)\,(\alpha_i \nabla_q \alpha_j^* - \alpha_j \nabla_q \alpha_i^*) \quad , \tag{10b}$$

and ∇_q is the component of the gradient (in $\vec{k}$-space) in the $\vec{q}$-direction. We may now insert (10) into (3), and use $\lim_{q\to 0} \omega_{q\sigma} = q\, C_\sigma(\hat{q})$ to write

$$\lim_{\vec{k}'\to\vec{k}} G_\sigma(\vec{k},\vec{k}') = \frac{1}{2\rho C_\sigma^{\,2}(\hat{q})} \left|\hat{\varepsilon}_{q\sigma} \cdot [\hat{q}\, V(o) + \sum_{i<j} \vec{A}_{ij}\, V(G_i-G_j)]\right|^2 \quad , \tag{11}$$

(Recall $G_\sigma(\vec{k},\vec{k}') \equiv \omega_{q\sigma}^{-1} \left|g_\sigma(\vec{k},\vec{k}')\right|^2$.) which depends on the direction of $\vec{q}$ and not on its magnitude, as claimed in (6).

Now the form (11) is valid for points $\vec{k}'$ inside the element of surface area associated with the initial point $\vec{k}$, and so we may calculate <u>their</u> contribution $\tau_{init}^{-1}(\vec{k})$ to the integral (4) for $\tau^{-1}(\vec{k})$ to very good accuracy, in a manner analogous to the derivation of the zero-temperature limit (7). The difference is that the radial integral (dq) is now truncated at the surface-element boundary $q(\theta)$, and does not extend to infinity as in (7).

$$\tau_{init}^{-1}(\vec{k},\varepsilon=0) = (\pi^2\hbar|\vec{v}|)^{-1} \sum_\sigma \int_0^{2\pi} d\theta G_\sigma(\theta) C_\sigma(\theta) \int_0^{q(\theta)} q^2 dq\, f\,(\hbar\omega_q/k_BT) \quad , \tag{12}$$

The radial integral may still of course be done analytically, and then the angular integral done numerically. As a result of the truncation $q(\theta)$, the contribution $\tau_{init}^{-1}(\vec{k})$ is accurate for all temperatures, and this guarantees that the total scattering rate

$$\tau^{-1}(\vec{k},\epsilon=0) = \tau_{init}^{-1}(\vec{k},\epsilon=0) + (\text{sum over all other mesh points } \vec{k}') \qquad (13)$$

is accurate both at zero temperature (where $\tau^{-1} = \tau_{init}^{-1}$ are both equal to (7)) and at higher temperatures where typical phonon wavevectors are sufficiently large that the mesh provides adequate angular resolution. The expression (13) may not be accurate for some intermediate temperature interval, depending on the mesh density near $\vec{k}$. Evaluating τ^{-1} at 5K intervals, we find apparent minor loss of accuracy only at 5 K, occuring at some of the Fermi surface points.

III. The Results.

Effective Mass Enhancements.

We first present results for the effective mass enhancement λ, since it is the simpler quantity to talk about. λ is plotted in Fig. 3 as a function of position $\vec{k}$ on the Fermi surface, for orbits indicated on Figs. 1 and 2. Note that the values 0.37-0.42 are characteristic of free-electron-like regions, and that localized deviations from this range of values occur on the ridges. On the second-zone ridges the deviation is an increase; on third-zone ridges (near the principal section) it is a decrease. Near the third-zone neck the situation is more complicated and λ is untypically large everywhere. Our interpretation of the behavior everywhere except near the neck is that the localized deviations arise from changes in the electronic mixing coefficients.

This is evidenced both by the localization to the ridges (the mixing coefficients are the only important quantities in (2) which vary on such a short scale), and by the antisymmetry between zones. The antisymmetry may be understood by first noting that near a given ridge, and sufficiently far away from the third-zone neck region, two of the four mixing coefficients are dominant in the wavefunctions. It follows that the product of the two dominant mixing coefficients on, say, a second zone ridge, has the opposite sign from the corresponding product on the third zone ridge. As a result, typical squared matrix elements in (3) exhibit opposite interference effects in the two zones, and these appear to be largely responsible for the localized deviations in λ.

In addition to these ridge-localized variations, there are also longer-range variations: λ is somewhat larger in the vicinity of X (the square region) that it is near L (the hexagonal region) on the second-zone surface. On the third-zone surface λ tends to become larger as one moves toward the neck region. These long-range variations seem to be related to the amount of umklapp scattering which can occur, from the region in question. The X-region of the second zone generally lies closer to a zone boundary than does the L-region, and so unklapp processes are available at smaller wavevector from the X-region. The entire third-zone Fermi surface lies near zone boundaries, but the neck region is nestled in the zone corner, and achieves near-contact with the second-zone surface. So it is not unnatural that the largest values of λ should occur there.

The results shown in Fig. 3 agree quite well with those of Leung (ref. 7). As pointed out by him, the contrasting behavior between second and third zones (in the short-range variations) is not obtained in a single-OPW calculation, as done for example by Leavens and Carbotte.[8] The long-range variations, at least on the second zone, do seem to emerge correctly from such a treatment. This partial agreement between single-OPW and multi-OPW calculations is consistent with our interpretation of short and long-range variations as 2-OPW and umklapp effects, respectively.

In Table II we compare certain calculated orbital averages of λ with those inferred from cyclotron resonance data. It is pleasing that the variations in λ between different third-zone orbits are in agreement. In Table III, we compare point-values of λ with those calculated by Leung, and measured by Doezema and Wegehaupt using the surface-Landau-level (SLL) method. The two calculations agree, but the measured values are consistently larger. Note, however, that the SLL values are also larger than the measured orbital averages (Table II). We cannot account for this discrepancy.

Relaxation Rates.

We are interested in the scattering rate τ^{-1} as a function of both $\vec{k}$ and temperature T. Anticipating a T^3-dependence in free-electron regions, we plot $\tau^{-1}T^{-3}$ as a function of T (Fig. 4), for several points on the second-zone surface indicated on Fig. 1. At very low temperatures the anisotropy is huge. In free-electron regions there is an initial T^3-behavior which is augmented above a certain threshhold by umklapp scattering. To show this we compare (Fig. 4c) the total scattering rate for points $\vec{k}$ in the hexagonal region, with

that contribution which arises from scattering only to other states $\vec{k}'$ in the same hexagonal region (to eliminate umklapp). Note that the umklapp onset temperature is reduced as the point $\vec{k}$ moves outward from the center (L) toward the zone boundary (K). Finally, as one approaches the ridge (Fig.4a), there is no longer a well-defined umklapp threshhold (the distinction between "normal" and "umklapp" is not always possible when 2-OPW states are involved); the quantity $\tau^{-1} T^{-3}$ starts out large and falls monotonically with increasing temperature. Viewed as a function of $\vec{k}$, $\tau^{-1}T^{-3}$ is sharply-peaked at ridges for low temperatures. As the temperature increases, the peaks broaden and the anisotropy washes out. The washing-out is accomplished by a reduction of $\tau^{-1}T^{-3}$ near ridges, accompanied by an increase in free-electron regions. This view is demonstrated in Fig. 5, where $\tau^{-1}T^{-3}$ is plotted as a function of $\vec{k}$, on the principal (110) orbit on the third-zone arm. The absence of flatness in the zero temperature plot reflects the absence of completely free-electron character in the wavefunctions. It is not surprising that there is no apparent umklapp threshhold.

The magnitudes of $\tau^{-1}T^{-3}$ are generally in good agreement with the measured ones (Table IV), particularly at the free-electron points X and L. Interestingly, the calculated 3d-zone orbital average is nearly independent of temperature for T<30 K, and quite close to the measured value. Near the U-point, however, the calculated temperature variations are quite dramatic; the value given in Table IV represents the plateau which exists between 10 and 30 K at the U-point (see also Fig. 4b). The experimental value may reflect the smaller values of $\tau^{-1}T^{-3}$ predicted below 10 K, as well as at neighboring $\vec{k}$-points (Fig. 4b). A further

possibility is that the experimental value results from the U'-point on the 3rd zone (the point indicated on the (110)- orbit of Fig. 5, at which the surface-normal is z-directed). The calculated values range between 2.2 and 2.9×10^7 $sec^{-1}K^{-3}$, which are closer to the measured value of 3.1. However, the calculated λ-value at U' is 0.35 (Fig. 3c), and thus in poorer agreement with the measured one (Table III), which makes this identification appear an unlikely possibility.

It would be interesting to confirm the predicted deviations from T^3 behavior. The most clear and easily-interpreted ones occur on the second-zone between L and K, as shown on Fig. 4a. The $\vec{k}$-space variations are smoother near the V_2-ridges than near the V_1-ridges because the former have less curvature ($V_2 \sim 3V_1$).

In a few of the $\tau^{-1}T^{-3}$ plots (Figs. 4b, c) there is a noticeable dip at 5K, which results from the graininess of the mesh. Where it exists, the dip is small and there is nevertheless possible a smooth interpolation between T=0 and the T≥10K points. With a finer mesh, the dip would occur at lower temperatures and be less pronounced. Because of practical calculational considerations, coupled with the limited availability of lifetime data, such an effort seems unwarranted at the present time.

IV. Concluding Remarks.

The values of the effective mass enhancements calculated here are consistent with those calculated previously by Leung,[7] even though the two calculations differ in their detailed treatment of electronic structure and in

their methods of Fermi surface integration. The calculated anisotropy exhibits the same trends found in both the surface-Landau-level data and cyclotron resonance data, even though the actual magnitudes of λ inferred from the two sets of data appear to be inconsistent with one other (as discussed in the previous section). The calculated values agree more closely with the cyclotron mass determinations. We have not calculated the entire Fermi surface average of λ required for comparison with the specific heat data, but Leung claims to have found fairly good agreement there.[13]

The agreement between measured and calculated scattering rates is pleasing. Agreement is particularly good at the X and L points, where because of the free-electron character of the wavefunctions, the T^3-coefficient depends on the form factor only at zero wavevector. Because of this it is not surprising that the coefficients are nearly the same at these two points. For the third zone (110)-orbital average, where τ^{-1} is nearly cubic in temperature, the agreement is quite good. There is a factor of two discrepancy, however, with the measured T^3-coefficient identified with the second-zone point U. Owing to the rapid variations of $\tau^{-1}T^{-3}$ with both T and $\vec{k}$ near this point, as well as the possible (but unlikely) confusion with the similar point U' on the third zone, one should perhaps not expect very close agreement for the U-point. Finally, the interpretation of data at such points would be facilitated if the predicted deviations from T3-behavior were observed. Such observations would provide a stringent test of the theory, and, in particular, of the use of simple electronic structure for treating the electron-phonon interaction.

References

*Work supported by the United States Energy Research and Development Administration through Grant No. AT(11-1)-2315.

†Present address: Department of Physics, Rensselaer Polytechnic Institute, Troy, New York, 12181.

1. V.F. Gantmakher, Rep. Prog. Phys. 37, 317 (1974).
2. R.E. Doezema and J.F. Koch, Phys. Cond. Matter, 19, 17 (1975).
3. J.W. Wilkins, Observable Many-Body Effects in Metals, (Nordita, 1968).
4. P.B. Allen, Proc. 12th Int. Conf. Low Temp. Phys., 1970, Academic Press of Japan, Tokyo (1970).
5. See for example J.E. Robinson and J.D. Dow, Phys. Rev. 171, 815 (1968).
6. N.W. Ashcroft, Phil. Mag. 8, 2055 (1963).
7. H.K. Leung, Ph.D. Thesis, McMaster University, Hamilton, Ontario, Canada (1974), unpublished.
8. See C.R. Leavens and J.P. Carbotte, Solid State Commun. 9, 75 (1971), and references contained therein.
9. R.E. Doezema and T. Wegehaupt, Solid State Commun. 17, 631 (1975).
10. D.K. Wagner and R.C. Albers, J. Low Temp. Phys. 20, 593 (1975).
11. N.W. Ashcroft, Physics Letters 23, 48 (1966).
12. In the actual calculation, the momentum-dependence of the form factor is accounted for by the addition of the term
$\hat{\epsilon}_{q\sigma} \cdot \sum_{i<j} (\vec{G}_i - \vec{G}_j)\, 2\mathrm{Re}(\alpha_i^* \alpha_j)\, q\, \nabla_q V(\vec{G}_i - \vec{G}_j)$ to (10a). This is omitted from the text for brevity.
13. Leung calculates the surface-averaged value $\overline{\lambda} = 0.43$, which compares reasonably with the specific heat value $\overline{\lambda}_{expt} = 0.38$. See ref. 7, and N.W. Ashcroft and J.W. Wilkins, Physics Letters 14, 285 (1965) for details.

Table Captions

1. Listed are our computed values of surface integrals representing the "specific heat" and "optical" effective masses, and the Fermi surface area. The free electron velocity v_o and surface area S_o are given for reference.

2. For extremal orbits lying in the designated planes we list the "apparent" mass enhancement, which is calculated by comparing the measured cyclotron mass with the value calculated without enhancement (i.e. "band" mass) as indicated, and the orbital mass enhancement calculated here.

3. "Point" values of λ, measured by the surface-Landau-level method, are compared with two sets of calculated values.

4. Listed for comparison are the calculated and measured values of $\tau^{-1}T^{-3}$ at three points on the second-zone surface, and averaged over the (110) extremal orbit (Fig. 5) of the third-zone arm. Theoretical values are taken for definiteness at zero temperature, except for the U-point, where instead the approximate plateau value characteristic of the temperature interval 10–30 K is recorded.

Table I.

surface integral	computed value
$\frac{m_{SH}}{m} = \frac{v_o}{S_o} \int \frac{dS}{\lvert\vec{v}\rvert}$	0.986
$S_o^{-1} \int dS$	0.79
$\frac{m}{m_{opt}} = (S_o v_o)^{-1} \int dS \lvert\vec{v}\rvert$	0.67

free-electron quantities: $v_o = 2.02 \times 10^8$ cm/sec

$S_o = 38.5$ Å^{-2}.

Table II.

orbit Γ	m_Γ/m		λ_Γ	
	measured cyclotron effective mass	band mass (Ashcroft)	apparent * enhancement	calculated enhancement
Zone 2				
(110)	1.20	0.871	0.38	0.42
(111)	1.29	0.95	0.36	0.42
Zone 3				
(110)	0.130	0.095	0.37	0.38
(001)	0.73	0.495	0.47	0.44
neck	0.091	0.0605	0.50	0.48

* $\lambda_\Gamma = m_\Gamma^{meas}/m_\Gamma^{band} - 1$, where $m_\Gamma^{band}/m = \frac{1}{\pi}\oint_\Gamma \frac{dk}{\hbar|\vec{v}|} = \frac{1}{\pi}\frac{dA_\Gamma}{d\varepsilon}$

Table III.

Effective mass enhancements

	measured (ref.9)	calculated	
		Leung (ref.7)	present
X	0.49	0.41	0.42
L	0.49	0.39	0.37
U	0.65	0.44	0.47

Table IV.

	$\tau^{-1}T^{-3}$ (10^7 sec^{-1} K^{-3})	
	calculated (eqn. 5)	measured
Zone 2 [a]		
X	0.40	0.41
L	0.38	0.39
U	6.0	3.1
Zone 3 [b]		
(110) extremal orbit	5.0 (to 5.5)	4.0

a. ref. 9: surface-Landau-levels

b. ref. 2: Azbel'-Kaner cyclotron resonance

Figure Captions

1a.) Second-zone Fermi surface.

1b.) Second and third-zone Fermi surface sheets shown together. The 1/48 th minimum symmetry element is shown for the second zone; the third zone consists of three such sets of arms.

1c.) Second-zone mesh shown in detail. Certain Fermi surface points are names after corresponding points of high symmetry in the zone. The point U is defined so that its normal is $\hat{x}$-directed, to enable later comparison with experiment. Unnamed points, indicated by dots, will also be referred to later.

2a. and b.) Two views of the minimum symmetry element of the third-zone surface. λ and τ^{-1} are later calculated along the indicated line segments.

3a.) Our computed values of λ shown along the two line segments KL and LUX indicated on Fig. 1c, which together comprise the (110) orbit on the second zone surface.

3b.) Plot of λ along segment XWK, or (100) orbit on second zone surface. Note the discontinuity at the contact point, which arises from the discontinuity in the mixing coefficients.

3c.) Plot of λ along line segments indicated.(Fig. 2) on the third-zone surface.

4a.) Plots of $\tau^{-1}T^{-3}$ as functions of temperature for points along second-zone segment KL, indicated on Fig. 1c. Plots correspond in increasing order to points encountered as one moves from L to K.

4b.) Plots of $\tau^{-1}T^{-3}$ for points along segment LUX (again see Fig. 1c.)

4c.) Umklapp effect for point L and the point approximately midway between L and K. For each point, the lower part of the plot corresponds to the restriction of the integration (2) to the hexagonal face.

5.) Plots of $\tau^{-1}T^{-3}$ versus arclength on the (110)-orbit of the third-zone arm (Fig. 2), for several values of the temperature.

6.) The orbital average of $\tau^{-1}T^{-3}$ as a function of T, for the orbit of Fig. 5. The zero-temperature value is recorded in Table IV.

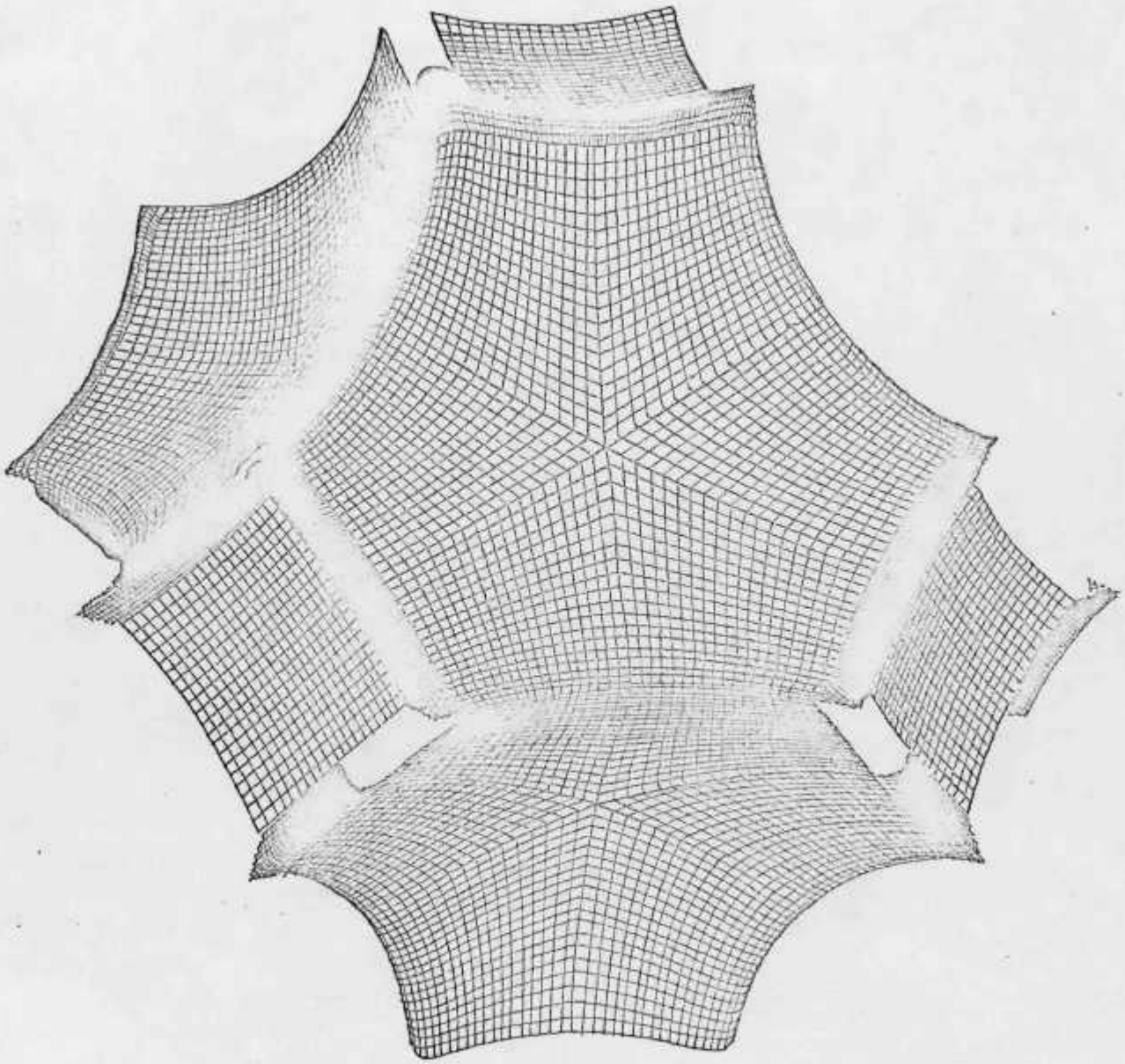

Figure 1a.

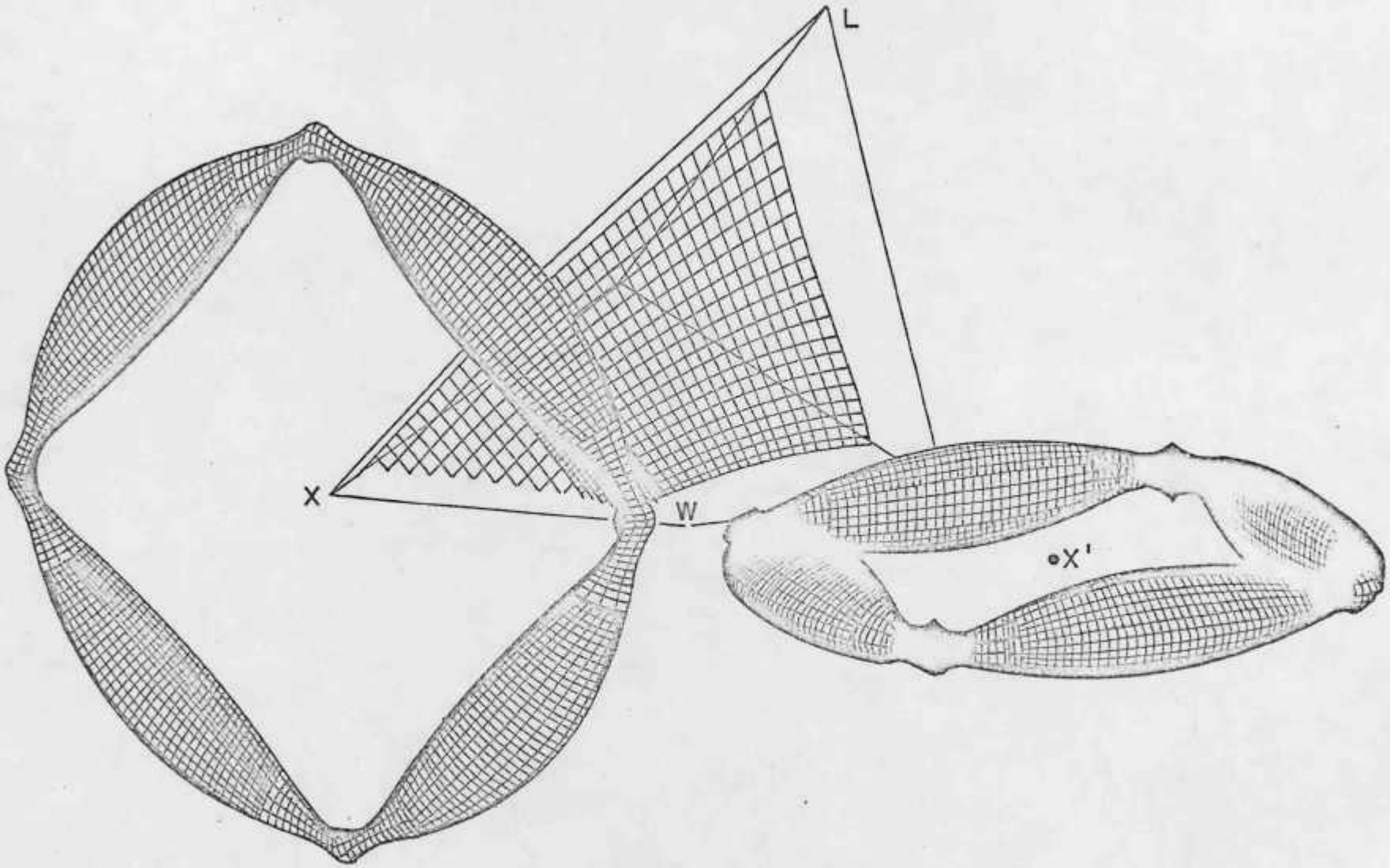

Figure 1b.

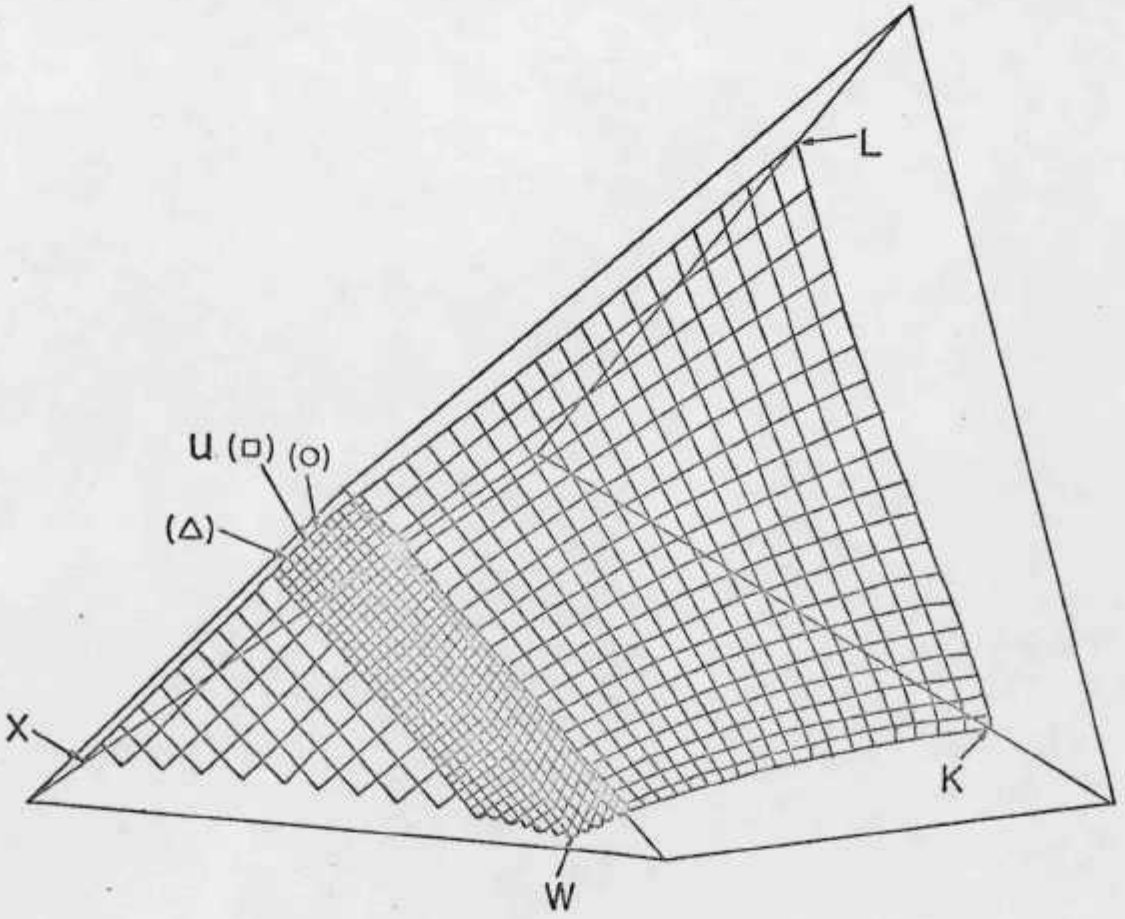

Figure 1c.

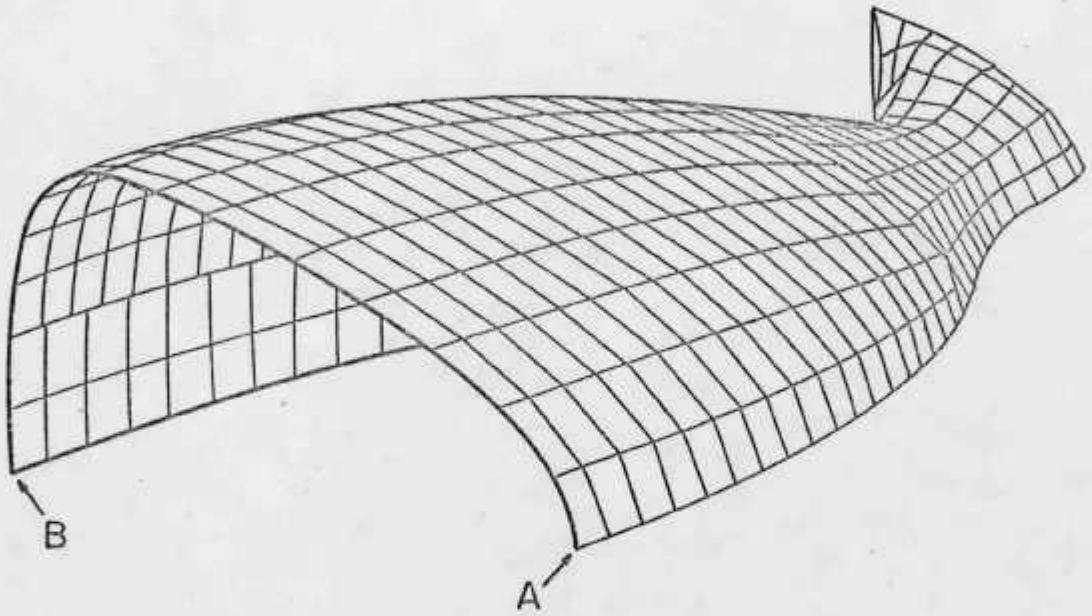

Figure 2a.

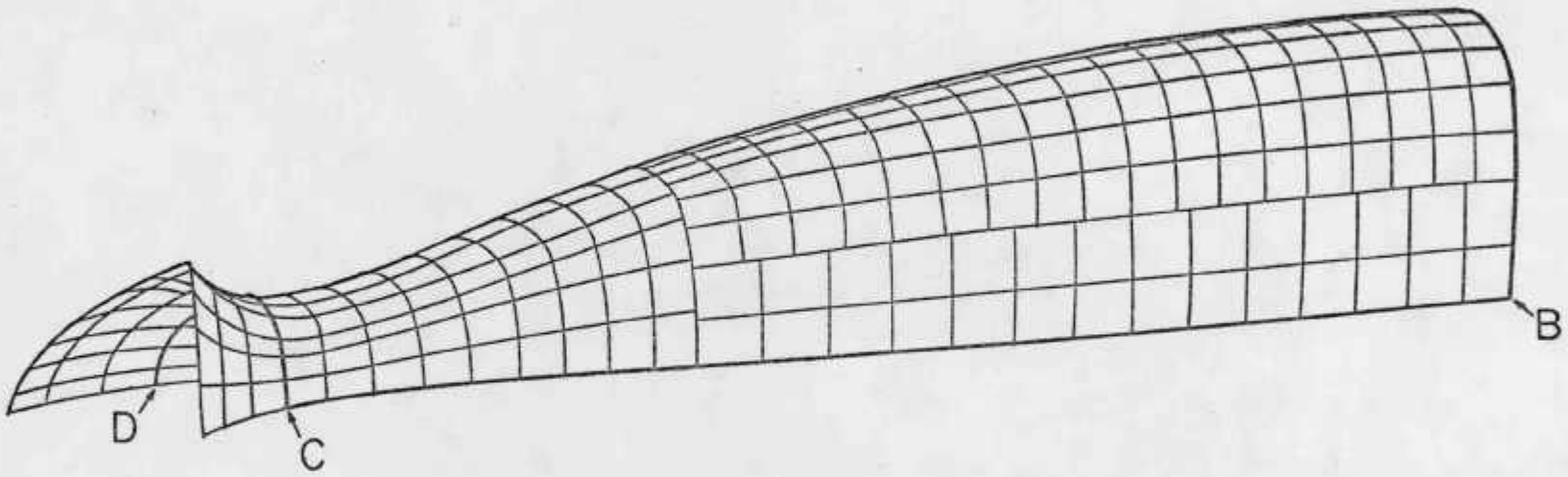

Figure 2b.

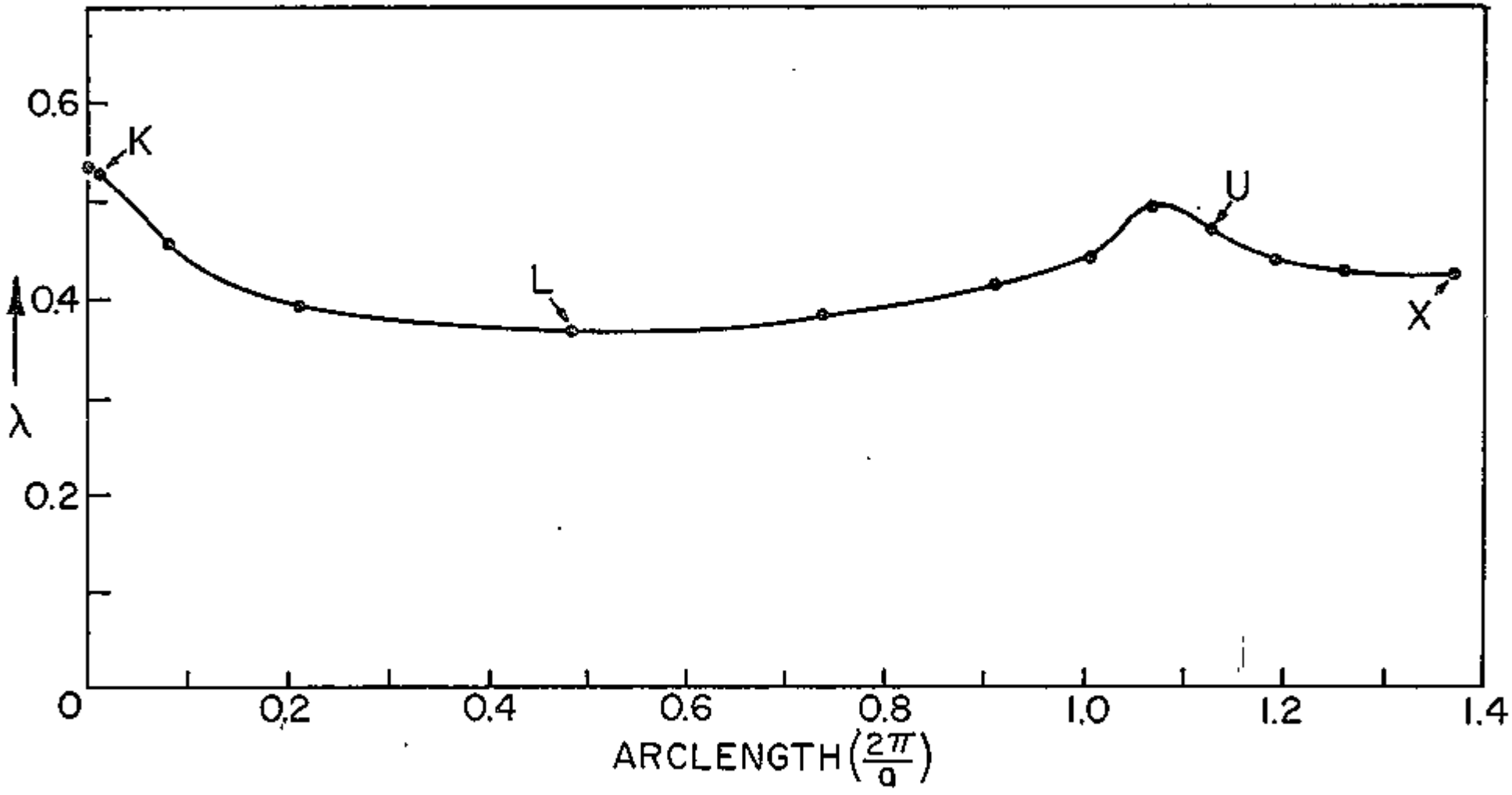

Figure 3a.

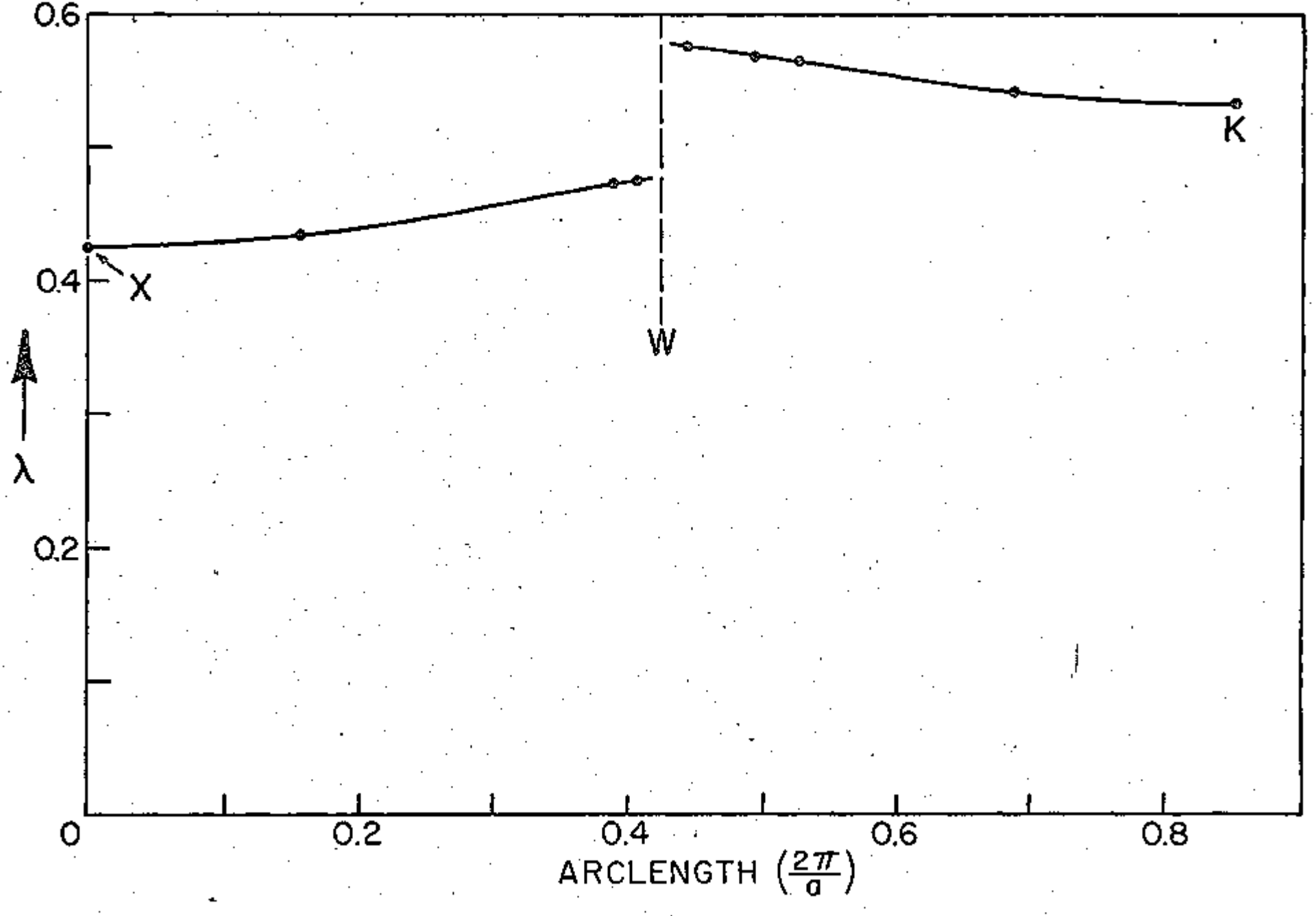

Figure 3b.

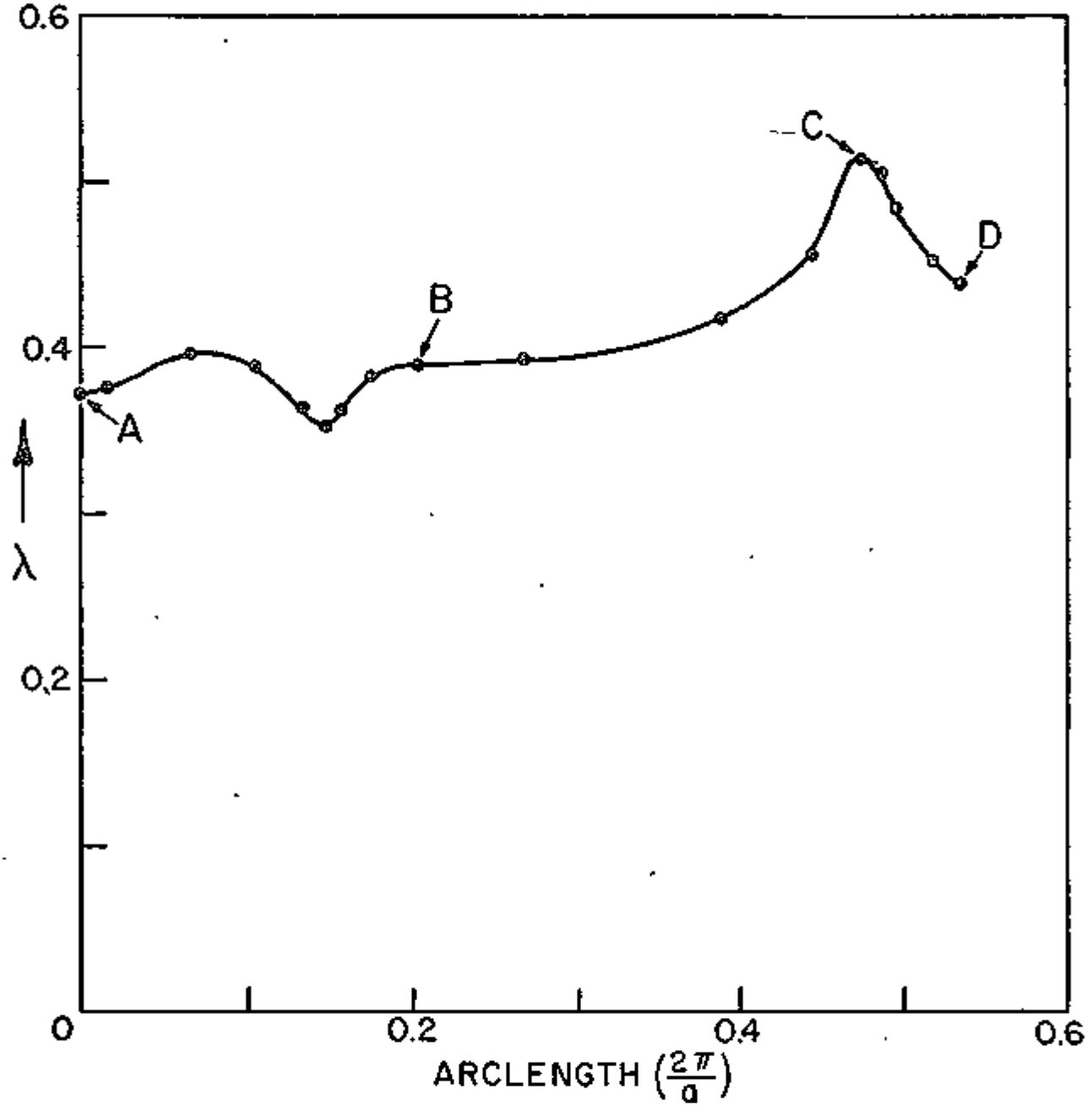

Figure 3c.

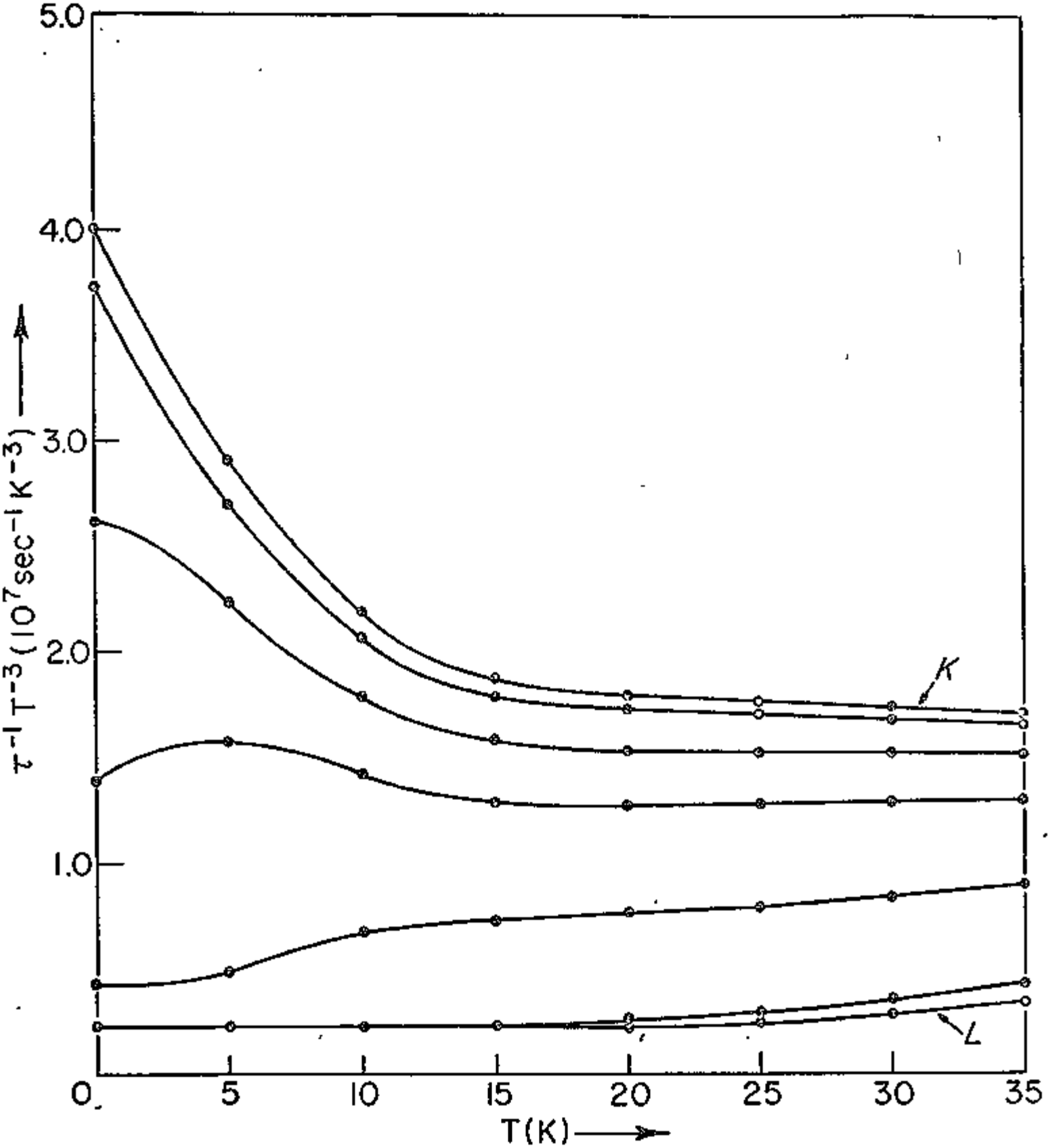

Figure 4a.

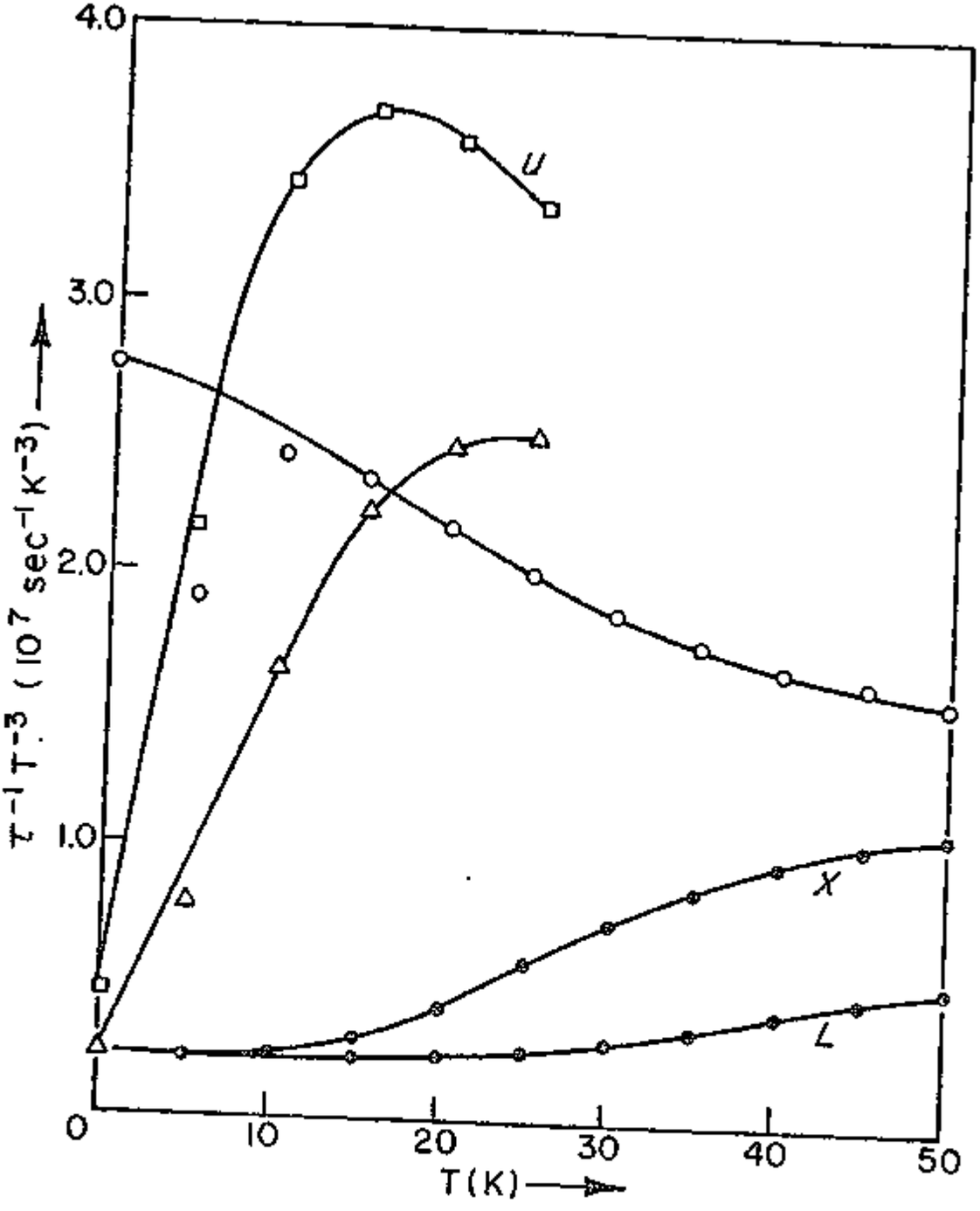

Figure 4b.

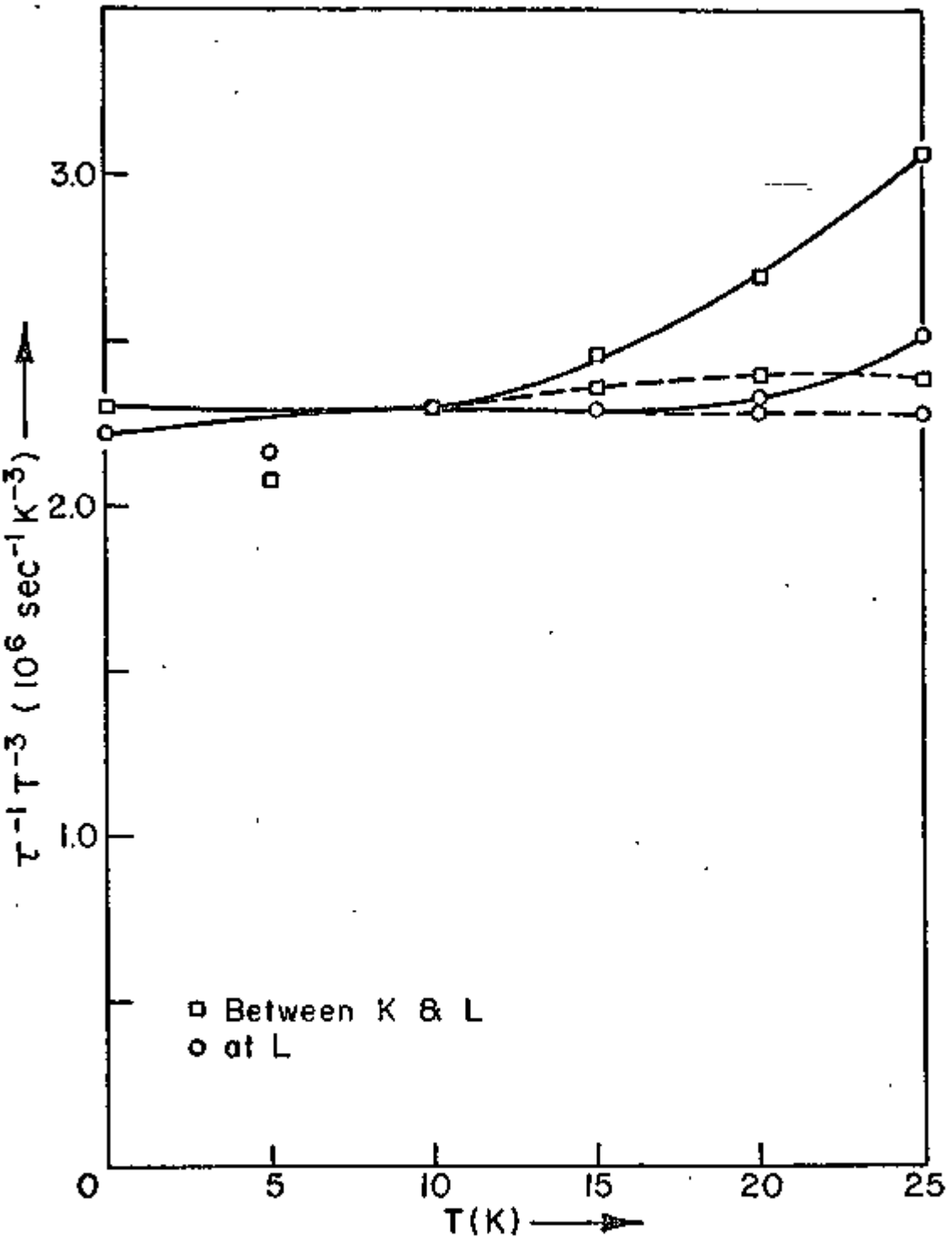

Figure 4c.

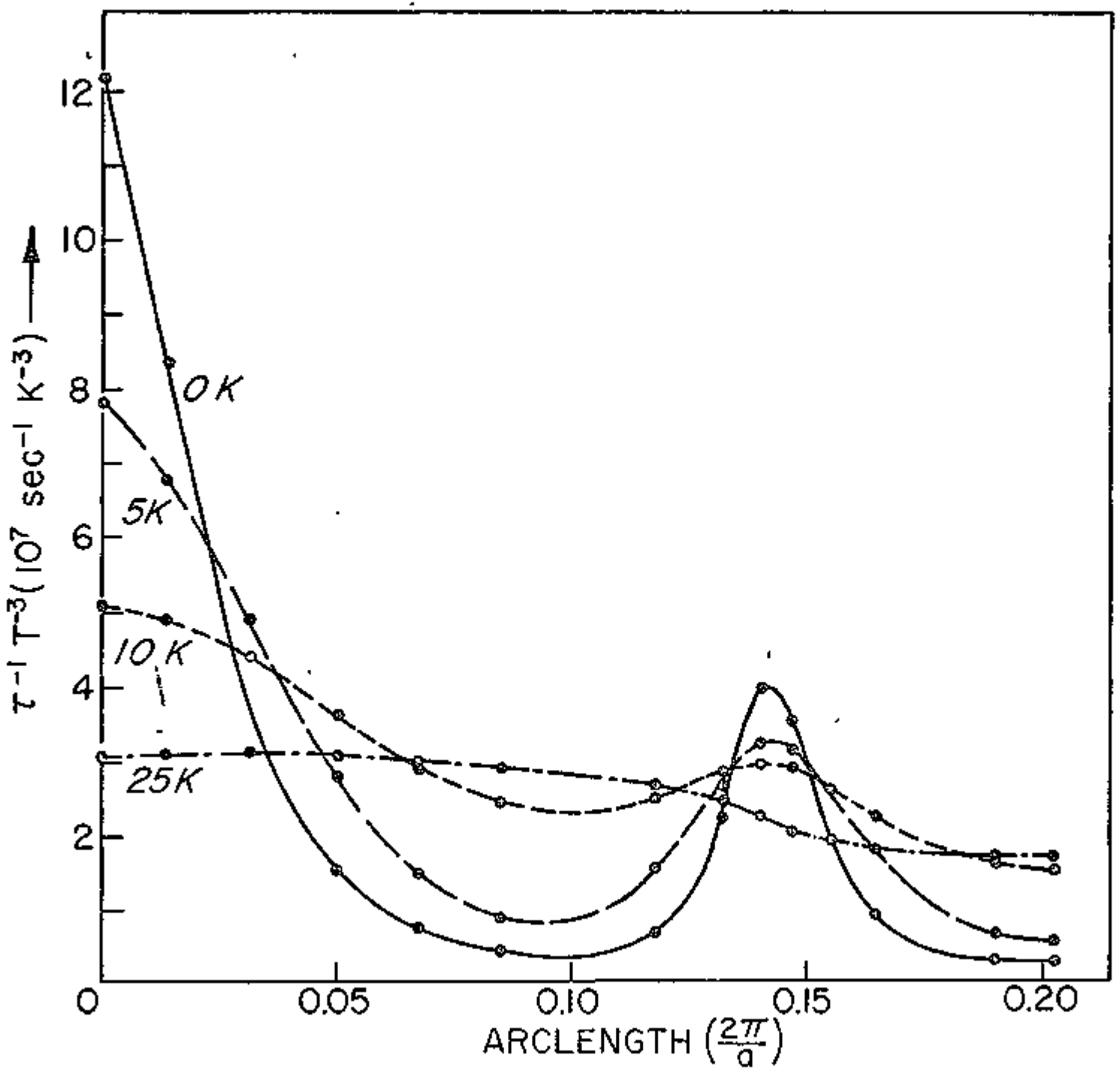
12
10
8
6
4
2
0
0.05
0.10
0.15
0.20
0 K
5K
10 K
25K
$\tau^{-1} T^{-3} (10^7 \text{ sec}^{-1} \text{ K}^{-3})$
ARCLENGTH $(\frac{2\pi}{a})$

Figure 5.

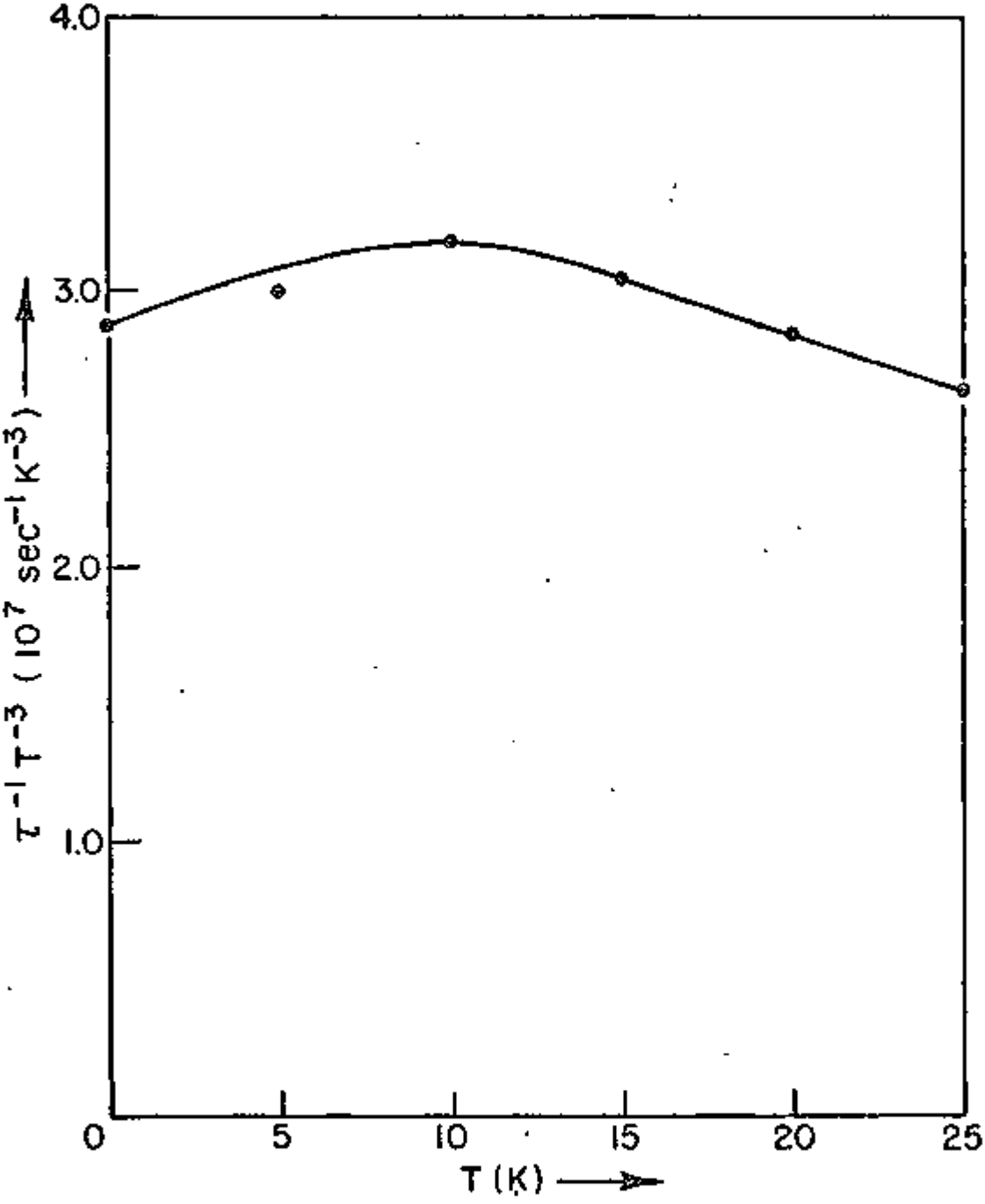

Figure 6.